Electron-capture-to-continuum cusp in U^{88+} + N$_2$ collisions

P.-M. Hillenbrand,[1,2,*] S. Hagmann,[1,3,†] D. H. Jakubassa-Amundsen,[4] J. M. Monti,[5] D. Banaś,[6] K.-H. Blumenhagen,[7,8]
C. Brandau,[1,2,9] W. Chen,[1] P. D. Fainstein,[10] E. De Filippo,[11] A. Gumberidze,[1,9] D. L. Guo,[12] M. Lestinsky,[1] Yu. A. Litvinov,[1]
A. Müller,[2] R. D. Rivarola,[5] H. Rothard,[13] S. Schippers,[2] M. S. Schöffler,[3] U. Spillmann,[1] S. Trotsenko,[1,7]
X. L. Zhu,[12] and Th. Stöhlker[1,7,8]

[1]*GSI Helmholtzzentrum für Schwerionenforschung, D-64291 Darmstadt, Germany*
[2]*Institut für Atom- und Molekülphysik, Justus-Liebig-Universität Giessen, D-35392 Giessen, Germany*
[3]*Institut für Kernphysik, Goethe Universität Frankfurt, D-60438 Frankfurt am Main, Germany*
[4]*Mathematisches Institut, Ludwig-Maximilians-Universität München, D-80333 München, Germany*
[5]*Instituto de Física Rosario, CONICET and Facultad de Ciencias Exactas, Ingeniería y Agrimensura,*
Universidad Nacional de Rosario, 2000 Rosario, Argentina
[6]*Institute of Physics, Jan Kochanowski University, PL-25-406 Kielce, Poland*
[7]*Helmholtz-Institut Jena, D-07743 Jena, Germany*
[8]*Institut für Optik und Quantenelektronik, Friedrich-Schiller-Universität Jena, D-07743 Jena, Germany*
[9]*ExtreMe Matter Institute EMMI and Research Division, GSI Helmholtzzentrum für Schwerionenforschung, D-64291 Darmstadt, Germany*
[10]*Centro Atómico Bariloche, Comisión Nacional de Energía Atómica and CONICET, 8400 San Carlos de Bariloche, Argentina*
[11]*Istituto Nazionale di Fisica Nucleare Sezione di Catania, I-95123 Catania, Italy*
[12]*Institute of Modern Physics, Chinese Academy of Sciences, Lanzhou 730000, China*
[13]*Centre de Recherche sur les Ions, les Matériaux et la Photonique, CIMAP-CIRIL-Ganil, F-14070 Caen, France*

For the collision system U^{88+} + N$_2$ at a collision energy of 90 MeV/u, the energy distribution of electrons being nonradiatively captured from the target into the projectile continuum has been measured under an angle of 0° with respect to the projectile beam axis. This measurement of the electron-capture-to-continuum cusp with the highest effective projectile charge $Z_p^{\text{eff}} = 88$ at a near-relativistic collision velocity of $\beta \approx 0.41$ is shown to be characterized by a strong asymmetry in the cusp shape. By comparing the data to measurements of the radiative-electron-capture-to-continuum cusp for the same collision system, the opposite asymmetry of the cusp is traced back to the varying underlying mechanisms. The experimental results are compared with the two theoretical calculations available for this process, one of them in the semirelativistic impulse approximation and the other in the nonrelativistic continuum-distorted-wave approach. A corresponding fully relativistic treatment may be motivated by the presented experimental data.

PACS number(s): 34.50.−s, 34.70.+e

I. INTRODUCTION

In ion-atom collisions, the surprisingly intricate features exhibited by differential cross sections for ionization of the target atom by the passing projectile ion have been and still are a continuous challenge for advanced theories. Over time, a very stimulating complexity of reaction channels became evident: Electrons ionized from the target atom are not only found in the target continuum, which is the dominant channel only for swift collisions and weak perturbations, but for stronger perturbations, the target electron may also be transferred into bound states of the projectile and notably even into the low-energy continuum states of the projectile.

The energy distribution of free electrons from the ionized target, which are prominently observed under forward emission angles $\vartheta_e \approx 0°$ with respect to the projectile beam, is shaped by three distinguishable dynamical mechanisms [1]: (i) the soft-electron peak is formed by slow electrons excited from a bound target state into a low-energy continuum state of the target atom, (ii) the cusp-electron peak at electron velocities similar to the projectile velocity, $v_e \approx v_p$,
is formed by target electrons captured into the low-energy continuum of the projectile, and (iii) the binary encounter peak at electron velocities $v_e \approx 2v_p \cos \vartheta_e$ is formed by target electrons scattered quasielastically in the Coulombic potential of the projectile.

As for process (i), the qualitative description of differential cross sections for single and even multiple ionization of the target atom by a perturbation originating from a swift charged projectile, be it electron, positron, or highly charged ion, has developed since the early times of quantum mechanics to a spectacular success of understanding the dynamics of ionization processes [2–5]. Theoretical treatments of the binary encounter process (iii) have exhibited unexpected but very rich features of diffraction in quasielastic electron-ion scattering [6–8]. However, the process (ii) is theoretically the most challenging, particularly for high atomic numbers of projectile and target, atomic numbers, Z_p and Z_t, and relativistic collision velocities. Its description requires one to deal with a two-center problem of an electron being transferred from an initially bound state of the target atom to a final low-energy continuum state of the projectile ion, and a fully relativistic theory for this process is not yet available.

The capture of a target electron into the projectile continuum can occur with or without emission of a photon. The respective cusp shape is a subtle indicator of the action of

*p.m.hillenbrand@gsi.de
†s.hagmann@gsi.de

the perturbing field [9]. The nonradiative electron capture to continuum (ECC) [10], also called electron Coulomb capture or mechanical capture to continuum, requires a large momentum transfer to the target atom in order to facilitate momentum balance during the electron transfer to the projectile continuum. As such, it is highly sensitive to the shape and the width of the target Compton profile. Its cross section increases with the atomic number of the target as Z_t^5 and decreases with the projectile velocity approximately as v_p^{-11} in the nonrelativistic regime [11,12]. In contrast, in radiative electron capture to continuum (RECC), also termed radiative ionization (RI), the excess energy is released by emission of a photon [9,13]. Due to the necessary coupling to the radiation field, RECC is weaker than ECC, but its cross section falls off less sharply with v_p than ECC. If the photon energy is not measured, RECC is independent of the Compton profile and scales (for neutral target atoms) linearly with Z_t, decreasing with velocity approximately as v_p^{-5} for high nonrelativistic velocities [9,11]. While ECC dominates the spectrum at low collision energies, the electron spectrum at higher collision energy is thus governed by RECC. The crossing energy E_{cr}, at which the cross sections of both processes are comparably large, is nearly independent of the effective projectile charge Z_p^{eff}, but strongly increasing with Z_t [12]. For electron capture to bound states, it was first estimated by Briggs and Dettmann to be $E_{cr} \approx 9$ MeV/u for $Z_t = 1$ [14].

Due to its dominance at low collision energies, ECC was already discovered experimentally in the 1960s by Rudd *et al.* in collisions of protons with gaseous targets at projectile energies up to 300 keV/u, when a surprisingly sharp-peaked energy distribution of electrons emitted under forward angles was observed [15]. The highest sensitivity to ECC was achieved when the emitted electrons were observed under an angle of $\vartheta_e = 0°$ with respect to the projectile beam [16,17]. The cusp-shaped peak of electrons emitted in a very narrow cone around the beam direction and with a velocity peaking at the projectile velocity was discovered. In the frame of the projectile, these electrons have an almost vanishing kinetic energy.

The first quantitative theoretical interpretation of ECC as capture of a single target electron to the projectile continuum was given by Salin [18] and Macek *et al.* [19,20]. The theoretical work of Shakeshaft and Spruch then illustrated the implications of ECC spectra for a deeper understanding of the underlying collision dynamics and the electron charge-cloud evolution during and after ionization [21–23]. In the 1970s and 1980s, ECC was experimentally studied with projectile ions of low and medium effective projectile charge and energies up to a few MeV/u at tandem accelerators, and its characteristic asymmetric line shape became visible, distinguishing it from the symmetric electron-loss-to-continuum (ELC) cusp [24–28]. More refined approaches were taken in studies of ECC as a function of the electron solid-angle acceptance [29], as a function of the impact parameter and the outgoing projectile charge state [30], and as a function of the target recoil-ion momentum [31]. It was shown that at collision energies below a few MeV/u, events seen as ECC originate not only from true one-electron ECC. Instead, for low collision energies, these events may be dominated by a two-electron transfer-ionization (TI) process, where one target

electron is transferred into a final bound state and the other one is transferred into a final low-energy continuum state of the projectile [26,28,30]. In all of these investigations of various collision systems, the collision energy was not yet high enough for ECC to compete with RECC, but for nonbare projectiles, ECC was already competing with ELC, i.e., the process releasing electrons from the projectile. Electrons arising from ELC can only be identified experimentally by application of a coincidence condition with the up-charged projectile [26].

Only with the advent of heavy-ion accelerators, such as SIS18 at GSI, could projectile energies beyond the crossing energy E_{cr} eventually be reached, thus entering the regime where radiative capture processes dominate over nonradiative capture processes. The radiative electron capture (REC) and the nonradiative capture (NRC) of an electron from the atomic target into a bound state of the projectile ion were then extensively studied at projectile energies of $E_p \approx 50$–360 MeV/u by Stöhlker *et al.* [32–35]. When using a nitrogen target, E_{cr} was experimentally shown to be around 90 MeV/u for total radiative and nonradiative bound-state capture cross sections [33]. However, the direct study of radiative and nonradiative capture into the projectile continuum at collision energies comparable to E_{cr} only became possible when the first magnetic forward-angle electron spectrometer was implemented in a heavy-ion storage ring. The first coincidence experiment with this spectrometer observing RECC was performed by Nofal *et al.* at a projectile energy of $E_p = 90$ MeV/u [13]. By theoretically comparing ECC and RECC, the two competing processes were predicted to have an opposite asymmetry in the electron distribution of the cusp, which clearly demonstrates the difference in the underlying mechanisms [9,12]. For the RECC, the asymmetry was shown to scale approximately with $Z_p^{eff}/\gamma v_p$, reaching very high values for high Z_p^{eff} and low v_p, and can thus best be studied using heavy highly charged projectile ions [9].

In this paper, we present a measurement of double-differential cross sections for ECC for very high Z_p^{eff} and near-relativistic collision velocity, simultaneously with RECC and ELC. The measurement was performed near the crossing energy E_{cr} for a nitrogen target using a projectile beam of U^{88+} at $E_p = 90.38$ MeV/u. The energy distribution of electrons emitted from the target into the forward emission angle $\vartheta_f = 0°$ with respect to the projectile beam was measured using the in-storage-ring magnetic electron spectrometer. Since the cross sections of both ECC and RECC scale with the effective projectile charge approximately as $(Z_p^{eff})^{2.5}$ [12], the utilized U^{88+} projectile beam guaranteed large absolute cross sections and highest sensitivity to the predicted opposite asymmetry of the cusp-electron energy spectrum. The experimental results presented in this paper show that the ECC and the RECC cross sections are comparably large at this collision energy. Furthermore, the observation of distinctly different energy distributions of these two electron-transfer processes illustrates the fundamental difference in the underlying physical mechanism. For the ECC spectrum, a comparison to theoretical calculations based on the impulse approximation with semirelativistic electron wave functions [9,12] and to nonrelativistic continuum-distorted-wave (CDW) calculations using relativistic kinematics [36–38] will be given, as there are no *ab initio* fully relativistic calculations to date. The

quantum-mechanical impulse approximation restricts the influence of the weak target field to the initial state and to the transition operator, while the final continuum state is governed only by the strong projectile field. The CDW theory seeks the most suitable partitioning of the perturbations in the description of the final electronic state, taking into account both the binding to the target as well as the continuum with respect to the projectile. The transition operator in the present CDW theory is a sum of kinetic energy and short-range contribution to the projectile field.

The paper is organized as follows: The experimental setup is shown in Sec. II, the data analysis is explained in Sec. III, an outline of the two theories is given in Sec. IV, and the results and discussion are presented in Sec. V.

II. EXPERIMENTAL SETUP

The experiment was performed at the heavy-ion accelerator facility of the GSI Helmholtzzentrum für Schwerionenforschung, where isotope-pure beams of (almost) all ion species in charge states up to bare uranium are routinely available. Details of the experiment, with the electron spectrometer installed at the Experimental Storage Ring (ESR), have been described in Refs. [39,40]. Briefly, a beam of berylliumlike U^{88+} was injected into the storage ring at 90.38 MeV/u and cooled by electron cooling. The ion beam was directed to intersect a supersonic gas-jet target of molecular nitrogen N_2. The number of injected ions of about 10^8 and a gas-jet target area density of around 10^{12} particles/cm^2 led to an average luminosity of the order of $L \approx 100$ b^{-1} s^{-1}.

As described, the process of ECC,

$$U^{88+} + N_2 \rightarrow U^{88+} + [N_2^+]^* + e^-,$$
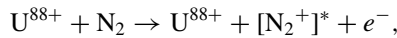
which is the focus of the current paper, is competing with RECC [40],

$$U^{88+} + N_2 \rightarrow U^{88+} + [N_2^+]^* + e^- + \gamma.$$
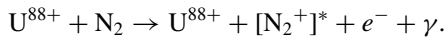
Since the projectile ions U^{88+} were not bare, projectile ionization, i.e., ELC [39],

$$U^{88+} + N_2 \rightarrow U^{89+} + [N_2]^* + e^-,$$

was additionally competing with the former two processes.

Electrons originating from these three processes, which were ejected from the interaction point at the gas-jet target into the forward direction, were measured by the electron spectrometer (Fig. 1). The spectrometer consisted of two $60°$ dipole magnets, each with an effective bending radius of 229 mm, and an iron-free quadrupole triplet in between the dipole magnets. The first $60°$ dipole located 790 mm downstream from the gas-jet target served both to magnetically separate the electrons from the ion beam and to analyze the momentum of the electrons. Through the combination of the first spectrometer dipole with the quadrupole triplet and the second dipole, an achromatic optics was realized in order to optimize the momentum as well as the angular acceptance of electrons being guided onto the position-sensitive electron detector. A combination of two microchannel plates in chevron configuration and a hexagonal three-layer delay-line anode was used as the electron detector. This provided redundant reconstruction information of the electron impact position
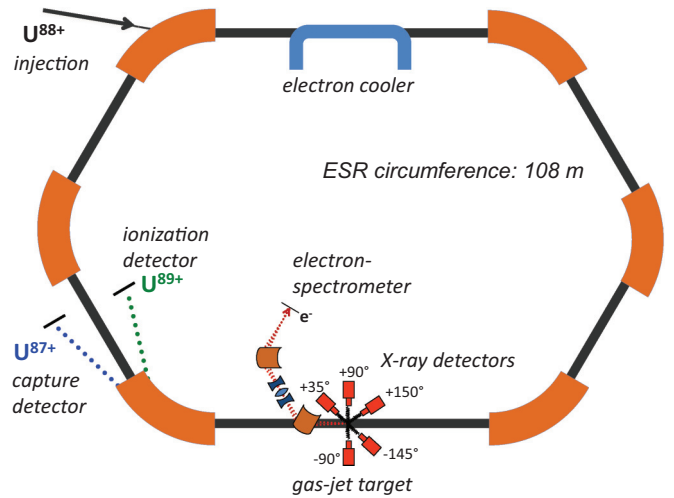

FIG. 1. (Color online) Layout of the experimental setup at the heavy-ion storage ring ESR with the electron cooler, the gas-jet target, the electron spectrometer, the x-ray detectors, and the particle detectors for projectile ionization and capture [40].

and considerably decreased dead time compared to a conventional rectangular delay-line anode [41]. The information of the electron impact position made sure that the electrons guided through the spectrometer were always well focused on the detector. The traveling distance for the electrons from the interaction point to the electron detector was 4.2 m, the diameter of the aperture was everywhere along its path >90 mm, and the diameter of the active area of the detector was 75 mm. The geometry and optics of the spectrometer permitted one to detect electrons emitted from the gas-jet target within the whole azimuthal emission angle of $\varphi_f = 0°–360°$ for a polar angle $\vartheta_f = 0° - \vartheta_{max} = 0°–2.4°$ with respect to the projectile beam axis, and a momentum spread of $\Delta p_e/p_e = 0.02$. These instrumental parameters were confirmed by electron optical calculations.

Projectile ions which lost or captured an electron while traversing the gas-jet target or the residual gas were magnetically separated from the primary projectile beam in the first ESR dipole behind the gas-jet target and, depending on their final charge state, detected in one of the two multiwire proportional chambers (MWPCs) located at suitable positions in the storage ring [42]. Around the gas-jet target, five high-purity germanium detectors were positioned at angles $\vartheta_\gamma = +35°, \pm 90°, -145°, +150°$ with respect to the projectile beam in the horizontal plane, in order to detect x rays emitted from the interaction point (Fig. 1) [40]. The MWPCs and the x-ray detectors were used to disentangle the contributions of the three competing processes to the electron cusp, as will be shown in the following section.

III. DATA ANALYSIS

The energy distribution of the cusp electrons was determined from the normalized number of events, N_e, detected in the electron spectrometer as a function of the magnetic field in the dipole magnets. After subtraction of background

events N_{bg}, e.g., from detector noise,[1] the number of events N_e represented the sum of the three contributing processes ECC, RECC, and ELC. All events $N_{e \wedge loss}$ originating from ELC could be determined by application of a coincidence condition between the electrons detected in the spectrometer and the up-charged U^{89+} projectiles detected in the corresponding MWPC, whose efficiency was close to 100% [42].

The events $N_{e \wedge \gamma}$ from RECC could be observed through a coincidence condition of electrons with the detected x rays [40]. In order to correct for the finite observation solid angle of the x-ray detectors in the order of $\Delta\Omega_\gamma \approx 10^{-3} \times 4\pi$ and the detection efficiency ϵ_γ, the events $N_{e \wedge \gamma}$ of electrons coincident with the x rays under $\vartheta_\gamma = +90°$ and $\vartheta_\gamma = -90°$ were extrapolated by multiplication with a factor $\lambda = \frac{1}{\epsilon_\gamma \Delta\Omega_\gamma} \frac{d^2\sigma}{dE_f d\Omega_f} / \frac{d^3\sigma(\vartheta_\gamma=90°)}{dE_f d\Omega_f d\Omega_\gamma}$ [33]. As described in Ref. [40], the photon angular distribution of RECC can be approximated by a $\sin^2 \vartheta_\gamma$ distribution, in which case the factor reduces to $\lambda = \frac{8\pi}{3} \frac{1}{\epsilon_\gamma \Delta\Omega_\gamma}$. To minimize uncertainties in the analysis, the experimental value of λ was determined individually for both x-ray angles by exploiting the fact, known from theory, that the cross section for ECC tends to zero at electron energies well above the cusp [9] (cf. Sec. V).

Therefore, the double-differential cross sections $d^2\sigma/dE_f d\Omega_f$ of ECC under the electron observation angle of $\vartheta_f = 0°$ as a function of the kinetic energy E_f were determined from the number N_e of counts on the electron detector, from which the background counts N_{bg}, the counts of electrons in coincidence with an up-charged projectile $N_{e \wedge loss}$, and the corrected number $\lambda N_{e \wedge \gamma}$ of electrons in coincidence with a photon were subtracted,

$$\frac{d^2\sigma^{ECC}}{dE_f d\Omega_f}\bigg|_{\vartheta_f=0°} = \frac{N_e - N_{bg} - N_{e \wedge loss} - \lambda N_{e \wedge \gamma}}{L_{int}}$$
$$\times \frac{1}{\epsilon_e \Delta\Omega_e} \frac{E_f + m_e c^2}{E_f^2 + 2E_f m_e c^2} \frac{1}{\Delta p_e / p_e}. \quad (1)$$

Here, the spectrometer efficiency is ϵ_e, the observation solid angle is $\Delta\Omega_e \approx \pi \vartheta_{max}^2$, and the relative momentum acceptance is $\Delta p_e / p_e$. The energy factor with the electron rest energy $m_e c^2$ includes both the conversion of momentum-differential to energy-differential cross sections dp_f/dE_f and the dispersion correction $1/p_f(\Delta p_e / p_e)$, i.e., the increasing absolute momentum acceptance with increasing momentum. The integrated luminosity L_{int} in units of b^{-1} is given by integration of the product of ion beam current $I_{ion}(t)$ and target area density $n_{target}(t)$ over the measurement time t:

$$L_{int} = \int \frac{I_{ion}(t) \, n_{target}(t)}{Z_p^{eff} e} dt, \quad (2)$$

with $Z_p^{eff} e = 88e$ being the projectile charge. In order to reduce uncertainties in the determination of L_{int} through Eq. (2), a normalization to the recombined U^{87+} ions detected in the corresponding MCWP was used.

_____

[1]The requirement to subtract the background (e.g., from detector noise) has always been the challenge in experimental investigations of ECC. It was also pointed out that it is deceptive to subtract a "physical" background [25], i.e., from seemingly competing processes.

The error bars were calculated by a quadratic summation of all relative systematic and statistical errors. For the determination of N_e, N_{bg}, and $\lambda N_{e \wedge \gamma}$, relative systematic errors of 5% each were assumed. This includes uncertainties in the reproducibility and energy dependence of the spectrometer efficiency while scanning its magnetic fields. In addition, the statistical errors of $N_{e \wedge loss}$ and $N_{e \wedge \gamma}$ were included.

Absolute cross sections were not derived from the data due to the uncertainty in the electron detection efficiency ϵ_e. Instead, the cross sections extracted from the experiment by applying Eq. (1) were normalized to theory. The normalization factor was determined as the weighted average of the ratio of experimental data and theory. While the experimental data was compared to two different theories (cf. Secs. IV A and IV B), the same normalization factor was used. However, the normalization for the data extracted for $\vartheta_\gamma = +90°$ and $\vartheta_\gamma = -90°$ was determined independently due to the different efficiencies and solid angles of the two x-ray detectors, ϵ_γ and $\Delta\Omega_\gamma$, respectively.

In a storage ring, the projectile velocity v_p of a cooled ion beam is given by the velocity of the electrons in the electron cooler [43]. Thus, for a given cooler voltage, the kinetic energy of the electrons in the cooler (corrected for space-charge effects) is the same energy as that for cusp electrons, when they travel with a velocity equal to the projectile velocity $v_e = v_p$. The space-charge corrected electron energy was $E_0 = 49.58$ keV. From this energy, the specific projectile kinetic energy of 90.38 MeV/u was deduced, as well as the projectile velocity in units of the speed of light $\beta = v_p/c = 0.4112$ or, in atomic units, $v_p = 137.036\beta = 56.33$ a.u., and the corresponding Lorentz factor $\gamma = 1 + E_0/(m_e c^2) = 1.097$, which are used throughout this paper.

The energy axis of the measured electron distribution was determined as follows: The magnetic field of the first momentum-analyzing dipole magnet of the spectrometer was measured on a relative scale with 10^{-3} relative uncertainty using a Hall probe. The momentum axis was converted into an energy axis and then calibrated using the ELC spectra measured simultaneously [39]. For this reason, beryllium-like projectiles U^{88+} were used in this experiment instead of bare projectiles U^{92+}. The ELC cusp has a quasisymmetric shape, such that its maximum is at E_0, independent of the precision to which E_0 is determined. Applying this *in situ* calibration method, the electron energy could be determined on an energy scale relative to E_0 with a precision of $\delta E_f/E_f = 0.01$.

IV. THEORY

A. Impulse approximation

The nonradiative electron capture to continuum from light target atoms to heavy, highly stripped projectiles can be calculated within the semirelativistic impulse approximation (IA). The characteristics of the IA are the treatment of the (weak) target potential V_t to first order in the transition operator while fully retaining the projectile field in the electron propagator. Also, off-shell effects are neglected. A full account of the IA for the ECC process is given in Ref. [12]. In a simplifying picture, this theory can be viewed as the Coulomb capture of a free electron with momentum $\boldsymbol{q}'$ into

a low-lying continuum state of the projectile, weighted with the momentum distribution of the initial target bound state. The transition amplitude is thus governed by the matrix element for Coulomb capture (in atomic units, $\hbar = m_e = e = 1$),

$$W_{\text{coul}}(\boldsymbol{q}', \boldsymbol{k}, m_s) = V_t(k) \int d\boldsymbol{r}' \psi^+_{\boldsymbol{p}'_f m_{s_f}}(\boldsymbol{r}') \, e^{i(\boldsymbol{k}_\perp \boldsymbol{r}'_\perp + \gamma k_z z')}$$

$$\times \left(1 + \frac{v_p}{c}\alpha_z\right)\psi_{\boldsymbol{q}' m_s}(\boldsymbol{r}'), \quad (3)$$

where $V_t(k)$ is the Fourier transform of the target field [which is $V_t(k) = -\sqrt{\frac{2}{\pi}} Z_t/k^2$ for a pure Coulomb field as chosen here]. The wave functions $\psi_{\boldsymbol{q}' m_s}$ and $\psi_{\boldsymbol{p}'_f m_{s_f}}$ describe, respectively, the intermediate and final projectile scattering states defined in the (primed) projectile frame of reference. They are characterized by the respective momenta $\boldsymbol{q}'$ and $\boldsymbol{p}'_f$ and the spin projections m_s and m_{s_f}. The z axis is chosen along the beam velocity $\boldsymbol{v}_p$ and α_z is a Dirac matrix. In contrast to the radiative electron capture, the ECC transition amplitude requires an extra integration over the momentum $\boldsymbol{k}$. Therefore, an additional transverse peaking approximation is convention-ally applied to evaluate this transition amplitude [12].

The characteristic feature of the ECC process, a cusplike divergence of the cross section when the electron is captured into the projectile continuum at threshold ($p'_f = 0$), arises from the normalization constant of the Coulomb scattering state $\psi_{\boldsymbol{p}'_f, m_{s_f}}$. This implies that the double-differential ECC cross section can be factorized according to

$$\frac{d^2\sigma}{dE_f d\Omega_f} = F_\eta \times \frac{d^2\sigma_{\text{rem}}}{dE_f d\Omega_f}, \quad (4)$$

where F_η is the absolute square of this normalization constant,

$$F_\eta = \frac{|N(\eta)|^2}{(2\pi)^3} = \frac{\eta}{4\pi^2(1 - e^{-2\pi\eta})}, \quad (5)$$

with

$$\eta = \frac{Z_p^{\text{eff}}(E'_f + m_e c^2)}{p'_f c^2} = \frac{\alpha Z_p^{\text{eff}}}{\beta'_f}. \quad (6)$$

Here, Z_p^{eff} is the asymptotic projectile charge (in case the projectile carries electrons) and $\alpha = 1/c$ is the fine-structure constant. Clearly, $F_\eta \to \infty$ for $p'_f \to 0$ (i.e., $\beta'_f \to 0$), while the remaining part of the cross section $d^2\sigma_{\text{rem}}/dE_f d\Omega_f$ in Eq. (4) is finite but discontinuous at $p'_f = 0$. When the Lorentz transformation to the target frame of reference is applied,

$$p_f \cos\vartheta_f = \gamma\left[p'_f \cos\vartheta'_f + \frac{v_p}{c^2}(E'_f + m_e c^2)\right],$$

$$p_f \sin\vartheta_f = p'_f \sin\vartheta'_f, \quad (7)$$

the location of the cusp at $E'_f = 0$ corresponds in the target frame to the electron emission angle $\vartheta_f = 0$ and $p_f = \gamma m_e v_p$.

In order to account for the finite angular acceptance ϑ_{max} of the electron detector (which renders the cusp finite), and for its momentum resolution $\Delta p_e / p_e$, the cross section of Eq. (4)

has to be averaged over ϑ_f as well as over E_f,

$$\left\langle \frac{d^2\sigma}{dE_f d\Omega_f} \right\rangle_{\vartheta_{\text{max}}, \Delta E_f} = \frac{1}{\Delta E_f} \int_{E_f - \Delta E_f/2}^{E_f + \Delta E_f/2} dE_f$$

$$\times \frac{1}{1 - \cos\vartheta_{\text{max}}} \int_0^{\vartheta_{\text{max}}} \sin\vartheta_f \, d\vartheta_f$$

$$\times \frac{d^2\sigma}{dE_f d\Omega_f}, \quad (8)$$

where the energy interval ΔE_f is related to the momentum resolution by means of $\Delta E_f/E_f = (\gamma + 1)/\gamma \times \Delta p_e/p_e \approx 2 \, \Delta p_e/p_e$ (and p_f is identified with p_e). For the evaluation of the ECC cross section, the transition matrix element given by Eq. (3) has to be convoluted with the momentum distri-bution of the target bound state [12]. For these target states, semirelativistic Darwin functions are used (see, e.g., [9]) with a Slater-screened effective charge and experimental binding energies. Taking into consideration that at the collision velocity $v_p = 56.33$ a.u., the capture yield of an L-shell electron is only about 4% of the K-shell capture yield, we have modeled the target L-shell electrons in terms of a spherical average over the magnetic quantum numbers, leading to an effective charge of 1.95 and a binding energy of 0.65 a.u. A crucial approximation consists, however, in the use of semirelativistic Sommerfeld-Maue (SM) wave functions for the electronic scattering states entering into the transition matrix element W_{coul}. With such functions, an analytic evaluation of the integral in Eq. (3), which is similar to the one occurring in the theory of bremsstrahlung, is possible [44,45]. For U^{88+}, which is treated as a bare nucleus with $Z_p^{\text{eff}} = 88$, or other heavy projectiles, the use of exact Dirac functions would be more appropriate since they do not underestimate the large momentum transfers involved. In contrast to the RECC process where such comparative studies were feasible [40,46], the evaluation of Eq. (8) with Dirac functions would involve an eightfold numerical integral over the highly oscillating and singular integrand from Eq. (3).

In fact, this integrand has a strong singularity near the cusp centroid, which gets less tractable with increasing Z_p^{eff}, and we had to resort, apart from using SM functions and the transverse peaking approximation, to two additional approximations. Instead of performing the angular average in Eq. (8), we have calculated $d^2\sigma/dE_f d\Omega_f$ at the fixed angle $\vartheta_f = 1.35°$, which provides a reasonable estimate for the average with $\vartheta_{\text{max}} = 2.4°$. Moreover, using the factorization in Eq. (4), we have calculated $d^2\sigma_{\text{rem}}/dE_f d\Omega_f$ in the wings of the cusp (i.e., for $|E_f - E_0| \gtrsim 2.5$ keV) and have interpolated it across the peak maximum, separately for K-ECC and L-ECC. The total ECC cross section per nitrogen atom is then obtained from

$$\frac{d^2\sigma^{\text{ECC}}}{dE_f d\Omega_f} = F_\eta \left[2\frac{d^2\sigma_{\text{rem}}^K}{dE_f d\Omega_f} + 5\frac{d^2\sigma_{\text{rem}}^L}{dE_f d\Omega_f}\right]. \quad (9)$$

Since the cross sections on the right-hand side of Eq. (9) are discontinuous at E_0 for $\vartheta_f = 0$, this interpolation is the more accurate (and the interpolation interval the smaller) the larger the chosen fixed angle ϑ_f in the evaluation of Eq. (4).

In Eq. (9), as everywhere in the present paper, the cross section is given per target atom. In fact, the collision energy is very large compared to the molecular binding energy of N$_2$,

such that the molecular character of the target can safely be neglected.

B. Continuum-distorted-wave model

The ionization of a target electron into the projectile continuum was also studied by means of extension of the continuum-distorted-wave (CDW) model to describe ionization by dressed projectiles. Such an extension has been used previously to compute double-differential cross sections for several systems, combining different projectiles colliding with He targets at intermediate-high impact energies [36–38]. The present theoretical model differs from that presented earlier by Monti *et al.* in the fact that relativistic kinematics was implemented in order to take into account the high collision velocity of the present system.

In order to treat multiple-electron systems within the independent electron model, we consider only one active electron and, following the procedure given in Ref. [47] (see also Refs. [1,48]), the multielectronic Hamiltonian is reduced to (in atomic units)

$$H_{\text{el}} = -\tfrac{1}{2}\nabla^2 + V_t(\boldsymbol{r}) + V_p(\boldsymbol{r}') + V_s(\boldsymbol{R}), \quad (10)$$

where $\boldsymbol{r}$ and $\boldsymbol{r}'$ are the positions of the active target electron in the target and projectile reference frames, respectively. The potential $V_t(\boldsymbol{r})$ contains the interaction of this electron with the remaining—partially dressed—target, and $V_p(\boldsymbol{r}')$ is the interaction between the projectile and the active electron that, according to the work presented in Refs. [36,37], is approximated with an analytical two-parameter Green-Sellin-Zachor (GSZ) potential [49–51]:

$$V_p(\boldsymbol{r}') = -\frac{Z_p^{\text{eff}}}{r'} - \frac{1}{r'}\big(Z_p - Z_p^{\text{eff}}\big)\big[H(e^{r'/d} - 1) + 1\big]^{-1}, \quad (11)$$

where $Z_p^{\text{eff}} = 88$ is the net (asymptotic) charge of the projectile, and $Z_p = 92$ is its nuclear charge. The parameters $H = 1.0277$ and $d = 0.0228$ a.u. are determined from Z_p and Z_p^{eff}. A detailed study showed that the application of a pure Coulomb potential $V_p(\boldsymbol{r}') = -Z_p^{\text{eff}}/r'$ instead of Eq. (11) does not significantly change the results of the CDW calculation for this collision system. These findings illustrated that the short-range part of the potential included in Eq. (11) does not play a significant role in the studied process.

In Eq. (10), the potential $V_s(\boldsymbol{R})$ is the mean interaction of the projectile with the target nucleus and the passive electrons. This potential depends only on the internuclear coordinate $\boldsymbol{R}(t) = \boldsymbol{b} + \boldsymbol{v}_p t$ with the impact parameter $\boldsymbol{b}$. Within the straight-line version of the impact-parameter approximation, the potential $V_s(\boldsymbol{R})$ produces a phase factor, which does not affect the electron dynamics.

The CDW approximation is the first order of a distorted-wave series. The initial and final distorted waves are defined as

$$\chi_i^+(\boldsymbol{r},t) = \Phi_i(\boldsymbol{r},t)\,\mathcal{L}_i^+(\boldsymbol{r}'),$$
$$\chi_f^-(\boldsymbol{r},t) = \Phi_f(\boldsymbol{r},t)\,\mathcal{L}_f^-(\boldsymbol{r}'). \quad (12)$$

Here, $\Phi_i(\boldsymbol{r},t) = \phi_i(\boldsymbol{r})\exp(-iE_i t)$ and $\Phi_f(\boldsymbol{r},t) = \phi_f(\boldsymbol{r})\exp(-iE_f t)$ are the initial-bound and final-continuum states

which are solutions of the time-dependent Schrödinger equations,

$$\left[-\frac{1}{2}\nabla^2 + V_t(\boldsymbol{r}) - i\frac{\partial}{\partial t}\bigg|_{\boldsymbol{r}}\right]\Phi_{i,f}(\boldsymbol{r},t) = E_{i,f}\Phi_{i,f}(\boldsymbol{r},t). \quad (13)$$

Also, $E_i < 0$ is the electron energy in the initial-bound state and $E_f > 0$ is the electron energy in the final-continuum state.

The initial distortion is defined as

$$\mathcal{L}_i^+(\boldsymbol{r}') = N(\nu)\,{}_1F_1(i\nu;\ 1;\ iv_p r' + i\boldsymbol{v}_p \cdot \boldsymbol{r}'), \quad (14)$$

whereas the final distortion is chosen as

$$\mathcal{L}_f^-(\boldsymbol{r}') = N^*(\eta)\,{}_1F_1(-i\eta;\ 1;\ -ip'_f r' - i\boldsymbol{p}'_f \cdot \boldsymbol{r}'), \quad (15)$$

where $\boldsymbol{v}_p$ is the projectile velocity, $\nu = Z_p^{\text{eff}}/v_p$, and $\eta = Z_p^{\text{eff}}/p'_f$. The ejected electron momentum in the projectile frame is $\boldsymbol{p}'_f$ as in Eq. (7), ${}_1F_1$ is the confluent hypergeometric function, and $N(a) = \exp(a\pi/2)\Gamma(1 + ia)$ is its corresponding normalization factor.

The N_2 initial-bound target molecular orbitals $\phi_i(\boldsymbol{r})$ of Eq. (12) are written as a linear combination of the atomic orbitals of the N atoms. Each atomic orbital is described by means of Roothaan-Hartree-Fock (RHF) wave functions [52]. The target final-continuum state $\phi_f(\boldsymbol{r})$ is chosen as a hydrogenic continuum state with an effective charge given by the prescription of Belkić *et al.* [53], i.e., $Z_t^{\text{eff}} = \sqrt{-2n^2 E_i}$, where n is the principal quantum number of the actual atomic orbital, and E_i is the energy of the corresponding molecular orbital. In order to provide a direct comparison to the theoretical results calculated via SM wave functions and to the experimental results, which are both given per target atom, the electron spectra resulting from the CDW calculations are presented in Fig. 2(b) as contributions to the molecular orbitals constructed from the dominating K-shell atomic orbital, constructed from the L-shell atomic orbitals, and the sum of both.

As was done for the IA calculation described in Sec. IV A, the electron spectra were calculated at the fixed angle $\vartheta_f = 1.35°$ instead of averaging over the spectrometer acceptance of $\vartheta_f = 0°$–$2.4°$. The results of the CDW calculation were also convoluted with the detector resolution.

V. RESULTS AND DISCUSSION

The results of the experiment, the double-differential cross sections $d^2\sigma/dE_f d\Omega_f$ of ECC for electrons emitted under an angle of $\vartheta_f = 0°$–$2.4°$ as a function of their kinetic energy E_f, are shown in Fig. 2: in Fig. 2(a) the experimental results are compared with the electron energy distribution calculated within the IA approach as described in Sec. IV A, and Fig. 2(b) shows the comparison with the electron energy distribution calculated within the CDW approach as described in Sec. IV B. It is seen that for both position and shape of the cusp, the experimental data are in reasonably good agreement with either theory. It is noteworthy that the two independent theoretical approaches give nearly the same absolute scale of the cross sections. The small differences in the cusp shape between both theories are comparable to the experimental uncertainty, such that the experimental data cannot discriminate the validity and accuracy of either theoretical model over the other for the studied collision system.
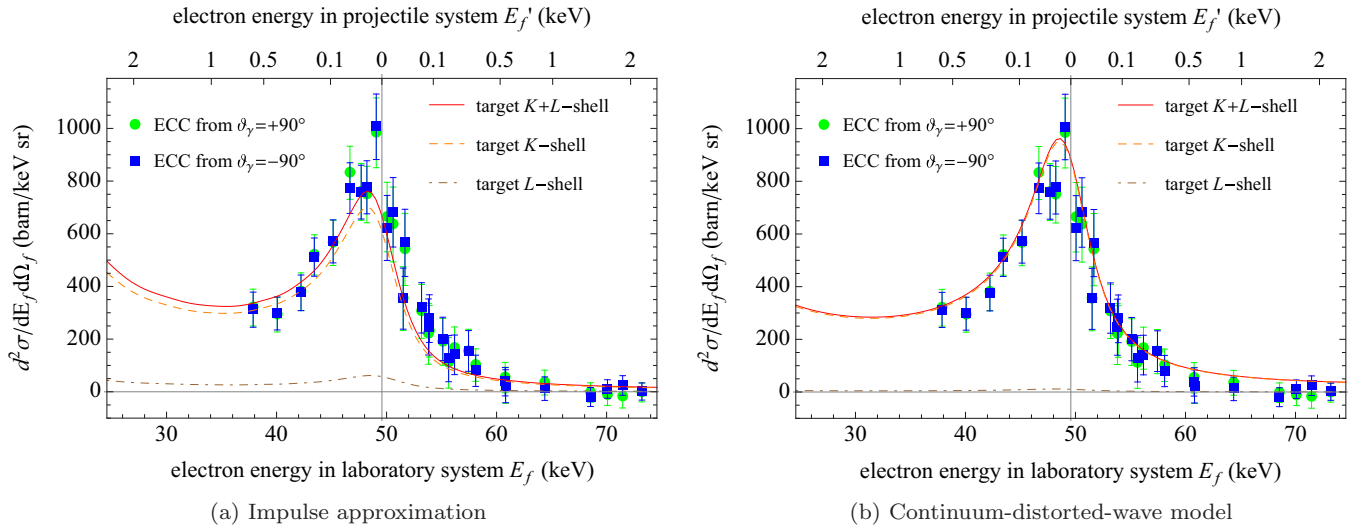
FIG. 2. (Color online) Energy distribution of electrons observed under an angle of $\vartheta_f = 0°$–$2.4°$ with respect to the projectile beam for the ECC. The experimental data were evaluated through Eq. (1) with the RECC events observed at $\vartheta_\gamma = +90°$ (green circles) and at $\vartheta_\gamma = -90°$ (blue squares), respectively. The two theoretical calculations show contributions of electrons from the nitrogen target K shell (dashed orange line), the nitrogen target L shell (dot-dashed brown line), and the sum of both (red solid line).

For energies $E'_f > 0.1$ keV $\approx E_0 \sin^2 \vartheta_{\max}$, the electron spectrum observed at small angles $\vartheta_f \approx 0°$ is almost independent of ϑ_f, since in the projectile frame the longitudinal component of the electron momentum $p'_{f_\parallel}$, which is measured by the spectrometer, is much larger than its unresolved transversal component $p'_{f_\perp}$. Therefore, this part of the spectrum does not depend on the boundary of the experimental integration interval $\vartheta_f = 0° - \vartheta_{\max}$ in Eq. (8), or on the choice of the scattering angle ϑ_f used in the theoretical calculation. In contrast, for energies $E'_f < 0.1$ keV, the longitudinal and the transversal momentum components of the emitted electron in the projectile frame are comparably large, $p'_{f_\parallel} \approx p'_{f_\perp}$, and the spectrum depends strongly on ϑ_f. In this energy range, experimental uncertainties may arise from an angle-dependent spectrometer efficiency, $\epsilon_e(\vartheta_f)$. Uncertainties in the theoretical calculations arise from the choice of ϑ_f, when the integration over the divergence, given by Eq. (8), is omitted. Variations of the theoretical calculations in the cusp spectrum resulting from the choice of ϑ_f are therefore restricted to electron energies at the cusp maximum with $E'_f < 0.1$ keV.

Within this experiment, the relative contribution of ECC in comparison with RECC and ELC was determined. The analysis of the RECC data has been discussed in detail in Ref. [40], and the analysis of the ELC data has been discussed in Ref. [39]. The relative experimental data presented in Fig. 3 indicate that the three processes contribute on a similar scale to the total electron cusp. The absolute scale has been chosen from the normalization of the ECC in Fig. 2. Here, the triply differential cross sections $d^3\sigma/dE_f d\Omega_f d\Omega_\gamma$ of RECC measured for $\vartheta_\gamma = +90°$ were extrapolated to the double-differential cross section $d^2\sigma/dE_f d\Omega_f$, integrated over all photon emission angles, by using the same factor λ as for the evaluation of the ECC cross section described in Sec. III.

In contrast to the experimental data, the calculated cross sections for the three processes deviate considerably from each other, and they also depend on the individual theoretical

approaches. The maximum of the ECC cusp when calculated as described above is a factor of six larger than the maximum of the RECC cusp if in both theories SM functions are used, while the corresponding factor is three for RECC calculated with exact Dirac waves [40]. Furthermore, the maximum of the theoretical ECC cross section is a factor of two larger than the maximum of the theoretical ELC cross section given in Ref. [39]. The discrepancy between the similar experimental cross sections for the three processes
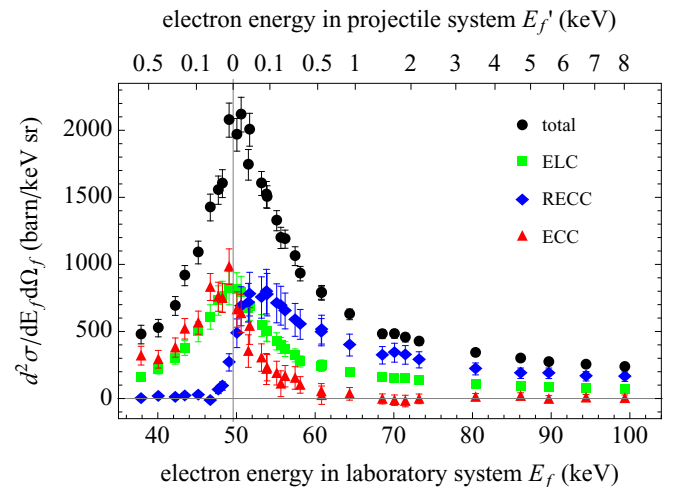

FIG. 3. (Color online) Energy distribution of electrons emitted under an angle of $\vartheta_f = 0°$–$2.4°$ with respect to the projectile beam: without any coincidence condition (black circles), i.e., background corrected singles, and individual contributions of nonradiative electron capture to continuum (red triangles), radiative electron capture to continuum (blue diamonds) [40], and electron loss to continuum (green squares) [39]. Here, the RECC data from $\vartheta_\gamma = +90°$ were used. The normalization determining the absolute scale of the cross sections was taken from Fig. 2.

and the different theoretical cross sections remains unresolved. It should be mentioned that the experimental data showing comparably large cross sections for ECC and RECC are consistent with the results of Ref. [33], where the crossing velocity for nonradiative and radiative electron capture to bound states (NRC and REC) was also found to be around 90 MeV/u for a nitrogen target.

A further analysis of the data revealed that the number of electrons detected in coincidence with a recombined projectile ion, $N_{e \wedge \text{cap}}$, was about three orders of magnitude smaller than the number of ECC events. Due to its small cross section, no spectra could be evaluated for the transfer-ionization process [26,28,30], $U^{88+} + N_2 \rightarrow U^{87+} + \left[N_2{}^{2+} \right]^* + e^-$, but the data indicate that for the collision energy studied here, transfer ionization is not significantly competing with the other three processes in the production of cusp electrons.

Concerning the spectral shape of the electron energy distribution, the experimental and theoretical results confirm the predicted strong asymmetry of the ECC cusp with a dominance of electrons at the low-energy slope $E_f < E_0$ [9]. The origin of this asymmetry can be explained in the following way. When the electron is transferred from the target atom to the low-energy projectile continuum, the longitudinal component of the momentum required to balance the released excess energy is shared between the target bound-state wave function (q_z) and the interaction potential (k_z). Within the impulse approximation—and neglecting the binding energy of the electrons in the target—the electron energy in the projectile frame E'_f is given by

$$E'_f = E_0 - \gamma v_p (q_z + k_z). \qquad (16)$$

For small energies in the projectile continuum ($E'_f \approx 0$), the required momentum can only be provided by electrons from the outer wings of the target Compton profile $J(q_z)$, combined with high Fourier components of the interaction potential. A decreased momentum transfer is therefore preferable, which leads to an increased energy of the electron in the projectile continuum $E'_f > 0$. Since there is no way for the scattered electron to lose energy, it is scattered quasielastically in the projectile potential and emitted under small forward angles in the projectile frame $\vartheta'_f \approx 0°$. In the laboratory frame for $\vartheta_f \approx 0°$, this corresponds to electron energies $E_f < E_0$ [39]. The ECC spectrum is therefore characterized by a smooth transition from the low-energy wing of the cusp down to the soft-electron peak, as discussed in Sec. I.

The theory shown in Fig. 2 clearly demonstrates that for ECC, the electrons dominantly originate from the strongly bound K shell of the nitrogen target which provides the required momentum transfer. We note that for the target K-shell electrons, a description within Slater-screened orbits is sufficiently accurate as compared to the Roothaan-Hartree-Fock orbitals. This is no longer the case for the L shell, the contribution of which is, however, small. According to the IA calculation, the contribution of nitrogen L-shell electrons to the cusp is about 8%, and according to the CDW calculation, it is about 1.5%. It is clear that both theories have problems describing the very small fraction of large-momentum components of the $2s$ and $2p$ wave functions, which are relevant in this case.

This behavior of large-momentum transfers of ECC can be contrasted to RECC, where the excess energy is transferred to an emitted photon of energy E'_γ,

$$E'_f = E_0 - E'_\gamma - \gamma v_p q_z. \qquad (17)$$

In this process, electrons from the whole range of the Compton profile participate equally. As can be seen in Fig. 3, the RECC cusp is characterized by electrons emitted predominantly with energies $E_f > E_0$. References [9,40] describe in detail that the emission of a hard photon goes along with a deeply inelastic scattering of the electrons in the vicinity of the projectile nucleus such that they are preferentially emitted into the backward direction in the projectile frame. In turn, this leads to the pronounced high-energy slope in the laboratory frame.

In the ELC process, the projectile ion is ionized through a weak perturbation that it experiences while passing the target atom [39]. The released electron is emitted almost isotropically in the the projectile frame, which leads to the observed quasisymmetric cusp shown in Fig. 3.

VI. SUMMARY AND OUTLOOK

The cusp-electron energy distribution of ECC has been studied both experimentally and theoretically for the collision system $U^{88+} + N_2$ at a projectile energy of 90 MeV/u. The experimental data are in good agreement with two independent calculations, one based on the impulse approximation and the other based on the continuum-distorted-wave model. It was experimentally confirmed that for heavy, highly charged projectiles, the ECC cusp is characterized by a strong asymmetry with a dominance of electrons observed with a velocity smaller than the projectile velocity. This behavior was experimentally shown to be opposite to the cusp-electron energy distribution for the competing RECC process. The comparison of both processes was rendered possible by choosing a projectile energy at which the cross sections of both processes are comparably large.

Improving the precision from the theoretical side would include a fully relativistic description of both the initial target bound states and the final projectile continuum states, and a nonperturbative two-center treatment of the electron dynamics [54–56]. This, however, has not been accomplished for ECC up to now.

To improve the precision of the ECC study from the experimental side, a bare, heavy, highly charged ion should be used as a projectile, with a kinetic energy well below E_{cr}, such that the competing processes ELC and RECC are suppressed. With the presented experimental setup, a coincidence measurement of the cusp electron and the down-charged projectile can also be performed, to study the two-electron channel of simultaneous electron capture to a bound and a continuum state of the projectile, i.e., transfer ionization, at near-relativistic collision energies [26,30]. A further important aspect of ECC is to investigate its impact-parameter dependence via coincidence measurement of the cusp-electron energy and the target recoil momentum, which requires the combination of the magnetic forward-electron spectrometer with a reaction microscope [57].

ACKNOWLEDGMENTS

[1] N. Stolterfoht, R. D. DuBois, and R. D. Rivarola, *Electron Emission in Heavy Ion-Atom Collisions*, Springer Series on Atomic, Optical, and Plasma Physics Vol. 20 (Springer, Berlin, 1997).

[2] F. Byron and C. Joachain, Phys. Rep. **179**, 211 (1989).

[3] C. W. McCurdy and F. Martín, J. Phys. B **37**, 917 (2004).

[4] J. S. Briggs and J. H. Macek, Adv. Atom. Mol. Opt. Phys. **28**, 1 (1990).

[5] I. E. McCarthy and E. Weigold, *Electron-atom Collisions*, Cambridge Monographs on Atomic, Molecular, and Chemical Physics, No. 5 (Cambridge University Press, New York, 2005).

[6] S. Hagmann, W. Wolff, J. L. Shinpaugh, H. E. Wolf, R. E. Olson, C. P. Bhalla, R. Shingal, C. Kelbch, R. Herrmann, O. Jagutzki, R. Dörner, R. Koch, J. Euler, U. Ramm, S. Lencinas, V. Dangendorf, M. Unverzagt, R. Mann, P. Mokler, J. Ullrich, H. Schmidt-Böcking, and C. L. Cocke, J. Phys. B **25**, L287 (1992).

[7] M. W. Lucas, D. H. Jakubassa-Amundsen, M. Kuzel, and K. O. Groeneveld, Int. J. Mod. Phys. A **12**, 305 (1997).

[8] C. Liao, S. Hagmann, C. P. Bhalla, S. R. Grabbe, C. L. Cocke, and P. Richard, Phys. Rev. A **59**, 2773 (1999).

[9] D. H. Jakubassa-Amundsen, J. Phys. B **36**, 1971 (2003).

[10] K. O. Groeneveld, W. Meckbach, and I. A. Sellin, in *Forward Electron Ejection in Ion Collisions*, Lecture Notes in Physics Vol. 213 (Springer, Berlin, 1984).

[11] J. Eichler, A. Ichihara, and T. Shirai, Phys. Rev. A **51**, 3027 (1995).

[12] D. H. Jakubassa-Amundsen, Eur. Phys. J. D **41**, 267 (2007).

[13] M. Nofal, S. Hagmann, T. Stöhlker, D. H. Jakubassa-Amundsen, C. Kozhuharov, X. Wang, A. Gumberidze, U. Spillmann, R. Reuschl, S. Hess, S. Trotsenko, D. Banas, F. Bosch, D. Liesen, R. Moshammer, J. Ullrich, R. Dörner, M. Steck, F. Nolden, P. Beller, H. Rothard, K. Beckert, and B. Franczak, Phys. Rev. Lett. **99**, 163201 (2007).

[14] J. Briggs and K. Dettmann, Phys. Rev. Lett. **33**, 1123 (1974).

[15] M. E. Rudd, C. A. Sautter, and C. L. Bailey, Phys. Rev. **151**, 20 (1966).

[16] G. Crooks and M. Rudd, Phys. Rev. Lett. **25**, 1599 (1970).

[17] K. Dettmann, K. G. Harrison, and M. W. Lucas, J. Phys. B **7**, 269 (1974).

[18] A. Salin, J. Phys. B **2**, 631 (1969).

[19] J. Macek, Phys. Rev. A **1**, 235 (1970).

[20] J. Macek, J. E. Potter, M. M. Duncan, M. G. Menendez, M. W. Lucas, and W. Steckelmacher, Phys. Rev. Lett. **46**, 1571 (1981).

[21] R. Shakeshaft, Phys. Rev. A **18**, 1930 (1978).

[22] R. Shakeshaft and L. Spruch, Phys. Rev. Lett. **41**, 1037 (1978).

[23] R. Shakeshaft and L. Spruch, Rev. Mod. Phys. **51**, 369 (1979).

[24] C. R. Vane, I. A. Sellin, M. Suter, G. D. Alton, S. B. Elston, P. M. Griffin, and R. S. Thoe, Phys. Rev. Lett. **40**, 1020 (1978).

[25] M. Breinig, S. B. Elston, S. Huldt, L. Liljeby, C. R. Vane, S. D. Berry, G. A. Glass, M. Schauer, I. A. Sellin, G. D. Alton, S. Datz, S. Overbury, R. Laubert, and M. Suter, Phys. Rev. A **25**, 3015 (1982).

[26] L. H. Andersen, M. Frost, P. Hvelplund, H. Knudsen, and S. Datz, Phys. Rev. Lett. **52**, 518 (1984).

[27] H. Knudsen, L. H. Andersen, and K. E. Jensen, J. Phys. B **19**, 3341 (1986).

[28] S. Datz, R. Hippler, L. H. Andersen, P. F. Dittner, H. Knudsen, H. F. Krause, P. D. Miller, P. L. Pepmiller, T. Rosseel, R. Schuch, N. Stolterfoht, Y. Yamazaki, and C. R. Vane, Phys. Rev. A **41**, 3559 (1990).

[29] W. Meckbach, I. B. Nemirovsky, and C. R. Garibotti, Phys. Rev. A **24**, 1793 (1981).

[30] A. Skutlartz, S. Hagmann, and H. Schmidt-Böcking, J. Phys. B **21**, 3609 (1988).

[31] T. Weber, K. Khayyat, R. Dörner, V. D. Rodríguez, V. Mergel, O. Jagutzki, L. Schmidt, K. A. Müller, F. Afaneh, A. Gonzalez, and H. Schmidt-Böcking, Phys. Rev. Lett. **86**, 224 (2001).

[32] T. Stöhlker, C. Kozhuharov, P. H. Mokler, A. Warczak, F. Bosch, H. Geissel, R. Moshammer, C. Scheidenberger, J. Eichler, A. Ichihara, T. Shirai, Z. Stachura, and P. Rymuza, Phys. Rev. A **51**, 2098 (1995).

[33] T. Stöhlker, T. Ludziejewski, H. Reich, F. Bosch, R. W. Dunford, J. Eichler, B. Franzke, C. Kozhuharov, G. Menzel, P. H. Mokler, F. Nolden, P. Rymuza, Z. Stachura, M. Steck, P. Swiat, A. Warczak, and T. Winkler, Phys. Rev. A **58**, 2043 (1998).

[34] T. Stöhlker, T. Ludziejewski, F. Bosch, R. W. Dunford, C. Kozhuharov, P. H. Mokler, H. F. Beyer, O. Brinzanescu, B. Franzke, J. Eichler, A. Griegal, S. Hagmann, A. Ichihara, A. Krämer, J. Lekki, D. Liesen, F. Nolden, H. Reich, P. Rymuza, Z. Stachura, M. Steck, P. Swiat, and A. Warczak, Phys. Rev. Lett. **82**, 3232 (1999).

[35] T. Stöhlker, X. Ma, T. Ludziejewski, H. F. Beyer, F. Bosch, O. Brinzanescu, R. W. Dunford, J. Eichler, S. Hagmann, A. Ichihara, C. Kozhuharov, A. Krämer, D. Liesen, P. H. Mokler, Z. Stachura, P. Swiat, and A. Warczak, Phys. Rev. Lett. **86**, 983 (2001).

[36] J. M. Monti, R. D. Rivarola, and P. D. Fainstein, J. Phys. B **41**, 201001 (2008).

[37] J. M. Monti, R. D. Rivarola, and P. D. Fainstein, J. Phys. B **44**, 195206 (2011).

[38] D. Fregenal, J. M Monti, J. Fiol, P. D. Fainstein, R. D. Rivarola, G. Bernardi, and S. Suárez, J. Phys. B **47**, 155204 (2014).

[39] P.-M. Hillenbrand, S. Hagmann, A. B. Voitkiv, B. Najjari, D. Banaś, K.-H. Blumenhagen, C. Brandau, W. Chen, E. De Filippo, A. Gumberidze, D. L. Guo, C. Kozhuharov, M. Lestinsky, Y. A. Litvinov, A. Müller, H. Rothard, S. Schippers, M. S. Schöffler, U. Spillmann, S. Trotsenko, X. L. Zhu, and T. Stöhlker, Phys. Rev. A **90**, 042713 (2014).

[40] P.-M. Hillenbrand, S. Hagmann, D. Atanasov, D. Banaś, K.-H. Blumenhagen, C. Brandau, W. Chen, E. De Filippo, A. Gumberidze, D. L. Guo, D. H. Jakubassa-Amundsen, O. Kovtun, C. Kozhuharov, M. Lestinsky, Y. A. Litvinov, A. Müller, R. A. Müller, H. Rothard, S. Schippers, M. S. Schöffler, U. Spillmann, A. Surzhykov, S. Trotsenko, N. Winckler, X. L. Yan, V. A. Yerokhin, X. L. Zhu, and T. Stöhlker, Phys. Rev. A **90**, 022707 (2014).

[41] O. Jagutzki, A. Cerezo, A. Czasch, R. Dörner, M. Hattas, M. Huang, V. Mergel, U. Spillmann, K. Ullmann-Pfleger, T. Weber, H. Schmidt-Böcking, and G. Smith, IEEE Trans. Nucl. Sci. **49**, 2477 (2002).

[42] O. Klepper and C. Kozhuharov, Nucl. Instrum. Methods B **204**, 553 (2003).

[43] H. Poth, Nature (London) **345**, 399 (1990).

[44] H. Bethe and L. Maximon, Phys. Rev. **93**, 768 (1954).

[45] G. Elwert and E. Haug, Phys. Rev. **183**, 90 (1969).

[46] D. H. Jakubassa-Amundsen and V. A. Yerokhin, Eur. Phys. J. D **67**, 4 (2013).

[47] P. D. Fainstein, V. H. Ponce, and R. D. Rivarola, J. Phys. B **21**, 287 (1988).

[48] P. D. Fainstein, V. H. Ponce, and R. D. Rivarola, J. Phys. B **24**, 3091 (1991).

[49] A. Green, D. Sellin, and A. Zachor, Phys. Rev. **184**, 1 (1969).

[50] P. Szydlik and A. Green, Phys. Rev. A **9**, 1885 (1974).

[51] R. Garvey, C. Jackman, and A. Green, Phys. Rev. A **12**, 1144 (1975).

[52] E. Clementi and C. Roetti, At. Data Nucl. Data Tables **14**, 177 (1974).

[53] D. Belkic, Phys. Rep. **56**, 279 (1979).

[54] K. Momberger, A. Belkacem, and A. H. Sorensen, Phys. Rev. A **53**, 1605 (1996).

[55] O. Busic, N. Grün, and W. Scheid, Phys. Rev. A **70**, 062707 (2004).

[56] Y. S. Kozhedub, V. M. Shabaev, I. I. Tupitsyn, A. Gumberidze, S. Hagmann, G. Plunien, and T. Stöhlker, Phys. Rev. A **90**, 042709 (2014).

[57] J. Ullrich, R. Moshammer, A. Dorn, R. Dörner, L. P. H. Schmidt, and H. Schmidt-Böcking, Rep. Prog. Phys. **66**, 1463 (2003).